

Strain-induced inflammation in pulmonary alveolar tissue due to mechanical ventilation

Parya Aghasafari¹ · Israr Bin M. Ibrahim¹ · Ramana Pidaparti¹

Received: 11 August 2016 / Accepted: 19 December 2016 / Published online: 13 February 2017
© Springer-Verlag Berlin Heidelberg 2017

Abstract Inflammation is the body's attempt at self-protection to remove harmful stimuli, including damaged cells, irritants, or pathogens and begin the healing process. In this study, strain-induced inflammation in pulmonary alveolar tissue under high tidal volume is investigated through a combination of an inflammation model and fluid structure interaction (FSI) analysis. A realistic three-dimensional organ model for alveolar sacs is built, and FSI is employed to evaluate strain distribution in alveolar tissue for different tidal volume (TV) values under the mechanical ventilation (MV) condition. The alveolar tissue is treated as a hyperelastic solid and provides the environment for the tissue constituents. The influence of different strain distributions resulting from different tidal volumes is investigated. It is observed that strain is highly distributed in the inlet area. In addition, strain versus time curves in different locations through the alveolar model reveals that middle layers in the alveolar region would undergo higher levels of strain during breathing under the MV condition. Three different types of strain distributions in the alveolar region from the FSI simulation are transferred to the CA model to study population dynamics of cell constituents under MV for different TVs; 200, 500 and 1000 mL, respectively. The CA model results suggests that strain distribution plays a significant role in population dynamics. An interplay between strain magnitude and distribution appears to influence healing capability. Results suggest that increasing TV leads to an exponential rise in tissue damage by inflammation.

Keywords Inflammation · Pulmonary alveolar sacs · Strain distribution · FSI · CA

1 Introduction

Inflammation is an immune response to tissue stimulation and is a complex process that involves diverse tissue constituents. It can be triggered by foreign matter entering the tissue, or a mechanical signal. Inflammation that occurs when mechanical ventilation (MV) is applied to support breathing in an alveolus environment is known to be induced by applied strain on the tissue, which may be caused by over-inflating the airways. In the case of MV, this leads to a dilemma—MV is necessary to maintain respiration, but it may also cause the lung to fail by inflammation-related problems. In particular, the pressure needed to maintain respiration under MV is more than normal breathing pressure. This is necessary to open presumed collapsed alveoli.

The mechanosensitive nature of pulmonary tissue has been known for a long time. Foda et al. (2001), focused on identifying major factors in the development of ventilator-induced lung injury. They demonstrated that high volume ventilation caused acute lung injury. Copland et al. (2003), studied the influence of high lung tidal volume and gene activation induced by mechanical stretch that occurs in the absence of physiologic or structural impairments in rat lung. They concluded that the pattern of gene activation that precedes high lung tidal volume-induced injury plays a significant role in the pathogenesis of high tidal volume-induced lung injury. Carnell et al. (2007), developed a histology-based methodology to explore the relation between intramural stress and combined monocyte/macrophage density and arteries branch elevation. They also tested the correlation between elevated stresses in hypertensive bifur-

✉ Ramana Pidaparti
rmparti@uga.edu

¹ College of Engineering, UGA, 132A Paul D. Coverdell Center, Athens, GA 30602, USA

cations and inflammation increase. They observed that cell density peaks appeared in regions where surface curvature would cause stress concentrations. They also concluded that there is a strong positive correlation between mean stress and cell density in each bifurcation.

Experimental studies (Li 2003; Li et al. 2004; Oudin and Pugin 2002) infer the mechanotransduction nature of lung tissue cells by statistical measurement of cytokines expression after they are subjected to stress. These results however, ignore factors such as strain level and distribution. There is also an issue of reproducibility where some cytokines are easily released in vitro but not in vivo. Several studies have shown that various cell signaling pathways were activated by subjecting pulmonary tissue to static or cyclic stretch. The cell signaling pathways during pulmonary tissue stretch may produce a number of proteins involved in inflammation, including p38 (Li et al. 2004; Uhlig et al. 2002), MAPK (Uhlig et al. 2002), IL-8 (Mascarenhas 2004), MMP-2 (Haseneen et al. 2003), ERK and NF-B (Birukov et al. 2003), MMP-9 (Pugin et al. 1998) and NOS (Kuebler et al. 2003), that are responsible for producing TNF, a well-known cytokine associated with inflammation. It is recognized that cytokines are redundant; hence, these cytokines may be released by the same triggers. These various cytokines would play different roles in inflammation; some would cause inflammation or dysfunction of other organs and are the precursor to biotrauma during MV. One way to study complex interactions between cells and cytokines in the pulmonary tissue environment is to treat the interaction as a discrete network. Insights might be gained from studying dynamics emerging from this interaction.

In this study, two different models are employed to study the strain-induced inflammation in the pulmonary alveolar tissue environment. First, a realistic three-dimensional (3D) organ model for alveolar sacs is built and fluid structure interaction (FSI) is employed to evaluate strain distributions in alveolar tissue under the MV condition. Alveolar tissue is treated as a hyperelastic solid and provides the environment for the tissue constituents. The tissue constituents are mechanosensitive cells that give rise to the dynamics at the cellular level by bio-chemical signaling. Second, a discrete network system modeled by Cellular Automata (CA) was used to represent the cellular model. Post-processed strain distributions from FSI are applied to the CA model to study population dynamics of cell constituents of tissue under the MV condition. The results obtained from both the models regarding the mechanical environment in alveolar tissue are discussed.

2 Materials and methods

To investigate the strain-induced inflammation in a pulmonary alveolar tissue environment, both fluid-solid interac-

tion (FSI) and cellular automata (CA) models are employed. A realistic 3D organ model for alveolar sacs is built, and hyperelastic material properties are assigned to the alveolar tissue. FSI is conducted to obtain strain distributions in alveolar tissue under MV condition. Appropriate boundary conditions are defined for FSI analysis and governing equations for fluid and solid domain are solved iteratively to obtain the strain distributions in alveolar tissue. These strains from FSI are applied to the CA model to study cell population dynamics of the tissue. Figure 1 presents an overview of the strain-induced inflammation model considered in this study.

2.1 Fluid solid interaction (FSI)

FSI studies that include both solid and fluid domains were used to investigate strain distributions in the alveolar region (Bungartz and Schfer 2006). A 3D realistic geometry of the alveolar region is created based on realistic dimensions (HaeffeliBleuer and Weibel 1988; Harding and Robinson 2010; Weibel 1964) and it is imported as geometry into the ANSYS transient structural and Fluent solvers. Constitutive equations for structure and fluid are integrated interactively in the time-domain, and structure displacement and fluid velocity and pressure are obtained iteratively. In each iteration, fluent transfers the fluid dynamic loads data to the transient structural solver at each pre-defined synchronization point and a transient structural solver transfers the structure response data to the FLUENT solver for the next iteration. These iterations are repeated until a maximum number of stagger iterations is reached or until the data transferred between solvers and all field equations have converged (ANSYS 2013). Strain distribution from FSI are post-processed for three different TVs and results for strain are employed for CA model.

2.1.1 Computational domain and boundary conditions

A 3D model of alveolar sacs is built with realistic dimensions. Shell element is considered for the solid domain and space inside the alveolar region is devoted to the fluid domain. The finite element converged mesh consists of 91,540 and 60,195 tetrahedrons and triangles for the fluid and solid domains, respectively. Neo-Hookean hyperelastic material properties with incompressible air are assigned to the alveolar wall and flowing fluid. In addition, pulmonary alveoli are the terminal ends of the respiratory tree, which contain some collagen and elastic fibers. The elastic fibers allow the alveoli to undergo strain as they are filled with air during inhalation. Then they spring back during exhalation in order to expel the carbon dioxide-rich air. Therefore, boundary conditions for the solid domain are allocated as free displacements in the radial direction for the model and longitudinal and rotational displacement are fixed for the simulation (Fig. 2; Table 1). Nonuniform inlet velocity boundary conditions for the fluid domain

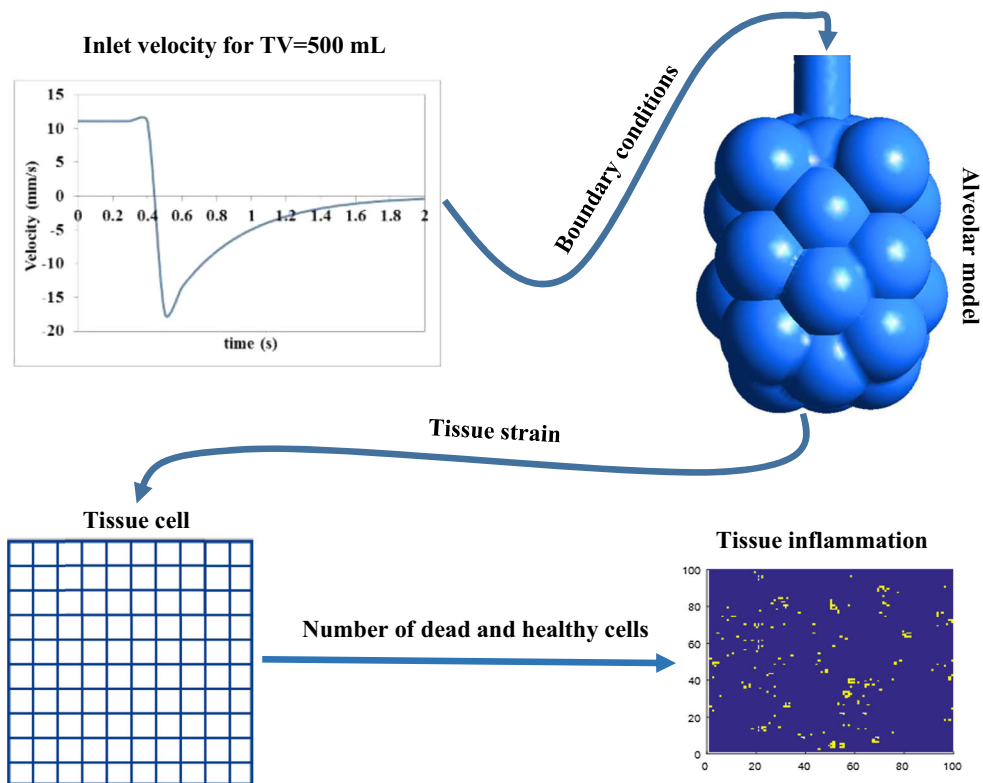


Fig. 1 Overview of strain-induced inflammation in this study

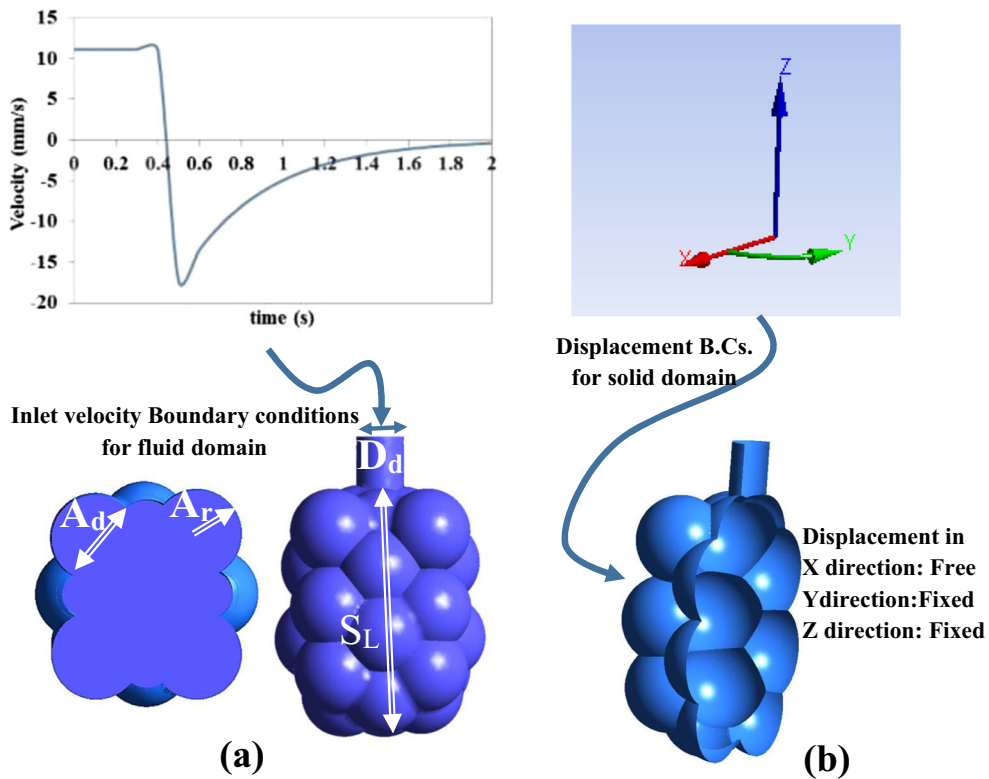


Fig. 2 Alveolar sac model geometry and B.C.s in the current study. **a** Fluid domain and **b** cut view of solid domain with shell element

Table 1 Alveolar sac model dimensions from the current study compared to morphometry reported in the literature

Parameters	Alveolar sac model current study	Dimensions literature review	References
Duct diameter (D_d) (mm)	0.19	0.25	HaefeliBleuer and Weibel (1988)
Alveolus radius (A_r) (mm)	0.15	0.14	Weibel (1964)
Alveolus depth (D) (mm)	0.2	0.23	Weibel (1964)
Sac length (SL) (mm)	0.87	0.75	HaefeliBleuer and Weibel (1988)
Number of alveoli	24	17	Weibel (1964)

Table 2 Inlet velocity wave form for MV

Inhalation/exhalation	MV
$t \leq$ Inhalation time (t_{in}) ($t_{in} \leq 0.4s$)	$\frac{Flowrate}{S*2^{(g-1)}}$
$t >$ Exhalation time (t_{ex}) ($0.4 < t_{ex} \leq 2s$)	$\frac{-Flowrate \times \exp\left(-\frac{t_{in}+t_{ex}}{t_{in}}\right)}{S*2^{g-1}}$

are defined in the form of constant and exponentially decreasing flow rate profiles for inhalation and exhalation during MV in the form of UDF files which are presented in Table 2.

where S is equal to the alveolar duct cross section, g is equal to the generation number which is equal to 23 in this study and flow rate is equal to the proportion of TV (lung volume that represents the normal volume of air displaced between inhalation and exhalation when extra effort is not applied) to the inhalation time. Three different values for TV (200, 500 and 1000 mL) are considered in the inlet velocity relationship to investigate their effects on increasing or reducing the damage in alveolar tissues under MV condition.

2.1.2 Governing equations for fluid

Since Reynolds numbers in the pulmonary sacs are generally sufficiently small (Clark et al. 2010; Kolanjiyil and Klein-streuer 2013), a 3D incompressible laminar Navier–Stokes and continuity equations in a 3D mesh domain with a control volume approximation (Liu et al. 2002) are solved numerically to give the velocity field within the alveolar region:

$$\nabla \cdot \mathbf{u} = 0 \quad (1)$$

$$\rho_f \left(\frac{\partial \mathbf{u}}{\partial t} + \mathbf{u} \cdot \nabla \cdot \mathbf{u} \right) = -\nabla p + \mu \nabla^2 \mathbf{u} \quad (2)$$

where \mathbf{u} is the velocity field, ρ_f is fluid density equal to $1.225 \frac{\text{kg}}{\text{m}^3}$, p is the pressure, and μ is the dynamic viscosity. The continuity equation represents the conservation of mass, Eq. (1), and the Navier–Stokes equations represent the conservation of momentum, Eq. (2), that would be solved numerically on a moving grid using a commercial finite-volume based program with fully implicit time marching techniques under isothermal conditions in ANSYS fluent solver (Fluent 2011).

2.1.3 Governing equations for structure

The governing equations for the movement of the alveolar sac walls during inhalation and exhalation are the time-dependent structural equations shown below:

$$\frac{\partial \sigma_{ij}}{\partial x_j} + \mathbf{F}_i = \rho_s \frac{\partial^2 u_i}{\partial t^2} \quad (3)$$

$$\sigma_{ij} = \mathbf{E}_{ijkl} \epsilon_{kl} \quad (4)$$

In the equations above is the stress in each direction, F is the body force, ρ_s is the density of tissue, u is the displacement, E is the elasticity tensor, and is the strain in each direction. Hyperelastic Neo-Hookean material parameters have been assigned to alveolar wall materials. Neo-Hookean hyperelastic materials have evolving nonlinear material properties and often used in large displacement applications (Tang et al. 2015; Wiechert et al. 2009). Neo-Hookean model with free energy density is adopted for FSI simulation in this study:

$$W = \frac{G}{2} (\bar{I}_1 - 3) + K_m (J - 1)^2 \quad (5)$$

where $J = \det(\mathbf{F})$ and $\bar{I}_1 = J^{-\frac{2}{3}} I_1$. I_1 is the first invariant of the left Cauchy–Green Tensor $\mathbf{C} = \mathbf{F}^T \mathbf{F}$ is the deformation gradient. G and K_m are the shear and bulk moduli, respectively. For this study $G = 2000$ (Pa) and $K_m = 13.5$ (kPa) are considered for Neo-Hookean parameters (Wiechert et al. 2009; Cavalcante et al. 2005). Also alveolar density is appointed as $196 \left(\frac{\text{kg}}{\text{m}^3} \right)$ (Gefen et al. 1999).

2.1.4 Coupling fluid-solid interactions

For each time step during FSI, initially Eqs. (1, 2) are solved and applied forces on the alveolar wall are calculated. Next, constitutive equations for solid are employed to obtain alveolar wall displacement. Then, the generated mesh is updated with the diffusion-based smoothing method in dynamic mesh in Fluent, based on the response of the structure. Interactions between solid and fluid are restated iteratively for optimization. Next, post-processed results from FSI are used

to investigate population dynamics of cells constituent of tissue under MV with different TVs in the cellular level model.

2.2 Cellular automata

CA is a discrete and rule-based model that has been used for both physics and biologic modeling. A well-known compilation of CA-oriented physical model is a work by [Chopard and Droz \(2005\)](#). They covered common physical model such as fluid flow, elastic solid, diffusion and reaction-diffusion. [Ermentrout and Edelstein-Keshet \(1993\)](#), compiled various CA model in biology. This works covered CA model built to give pattern commonly found in biologic system. The models built based on description of the components and interactions in associated biologic system. Recent application of CA includes cancer spread modeling ([Alemani et al. 2012](#)), disease infection ([Precharattana and Triampo 2014](#)) and inflammation ([Reynolds et al. 2012](#); [Brown et al. 2011](#); [Dutta-Moscato et al. 2014](#)). These models consist of several agents that interacts to give rise to the dynamics of the environment. [Reynolds et al. \(2012\)](#), defined several agents in the model that represent epithelium and macrophages with finite states. These agents change states according to environmental interactions. Other studies would provide further information on possible agents definition on CA model [Brown et al. \(2011\)](#), [Dutta-Moscato et al. \(2014\)](#). A CA model typically consists of a set of uniform cells (or agents), space represented by grids, and rules that define the cells behavior. The cells can be seen as mini-computer that computes the rules. Mathematically, a CA is defined in terms of set theory as a tuple:

$$A = \{G, E, U, f\} \tag{6}$$

where G, E, U and f are a grid of cells, set of finite states of cells, set of neighborhood and set of local rule, respectively. The grid is typically defined as d -dimensional square grid, that is $G = Z^d$. The state is typically defined as a finite set of numbers (e.g., binary, real). There is various definition of neighborhood, one of the most used is Moores neighborhood, defined as $U(x_i) = \{x \mid \|x_i - x\|_\infty \leq 1\}$. The local rule defines the evolution of state. The general form of rule is,

$$z^{t+1}(x) = f(z^t |_{U(x)}) \tag{7}$$

where $z^t(x)$ is state at x at time step t , and $z^t |_{U(x)}$ is state at the neighborhood of x . Finally, there needs to be a map from grid to states before applying the rules, that is $z : G \Rightarrow E$. One of the most common forms of local rules in CA is employing conditionals, which can also be represented as step function,

$$z^t = \begin{cases} 1, & \text{if } (A) \\ 0, & \text{else} \end{cases} \tag{8}$$

where A is conditional statement(s). The conditional statements typically involve the states of neighbors. Other recurring local rule is the summation of states,

$$z^{t+1}(x) = f(z^t |_{U(x)}) \tag{9}$$

Throughout this study, these two general forms of rule are used which are discussed in results and discussion section. The boundary of CA grid can be defined by two conditions: fixed or periodic. Fixed boundary condition imposes a constant value on the boundary. Periodic boundary lends itself from molecular modeling, and is used to approach large domain. It imposes continuum between two opposite facing boundaries. This condition can also be seen as a domain which satisfies torus topology.

2.3 Inflammation model

As it was discussed, inflammation is a complex process that involves the release and spread of cytokines and cells interaction with the environment. That is to say, inflammation is mainly the interplay between reaction–diffusion (R/D) of cytokines and cells response. To model this process, a discrete computational method based on cellular automata (CA) is employed ([Mascarenhas 2004](#)). The CA has been successfully applied to model behavior biologic system ([Tanabe et al. 2000](#)), including reaction diffusion and cells response and arrangement to environment, inflammation ([Birukov et al. 2003](#); [Moriyama 2004](#); [Uhligh and Uhligh 2001](#)) and cancer modeling ([Haseneen et al. 2003](#)). The discrete model employed in this study is largely based on probability. As usual, the CA model is built upon a definition of the grid. In this study, a square two-dimensional grid is used. The grid consists of several layers, as can be found in R/D modeling. There are four layers of grid: epithelial cells, immune cells (cells with motility), cytokines, proteins and elastic field grid. As per CA modeling, the evolution of the grids is dictated by a set of rules. The rules and grids are explained below. [Figure 3](#) illustrates the CA model with multiple grids, as well as a graph showing the causal path of the CA model.

2.3.1 Epithelial cells grid

The epithelial cells grid is a typical CA grid, with only two states: 1 and 0, representing dead and healthy, respectively. The rule that defines evolution of the CA cells in this grid is,

$$z_1^{t+1}(x) = \begin{cases} 1, & \text{rand}(\alpha_1, \beta_1) < z_{3TNF}^t(x) \\ 0, & \text{otherwise, or healing} \end{cases} \tag{10}$$

$$z_1^{t+1}(x) = \text{samp}(d, w) \tag{11}$$

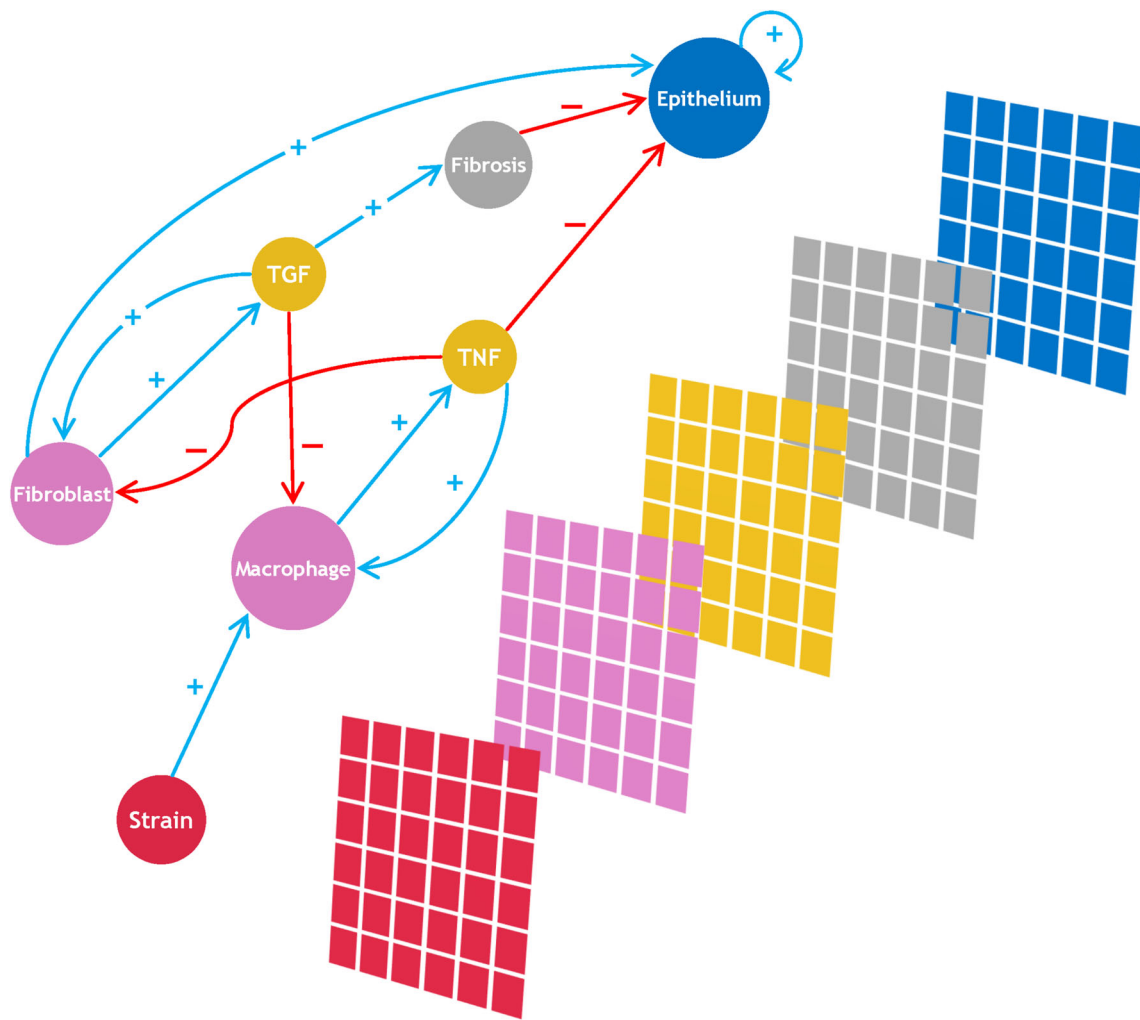


Fig. 3 CA with multiple grids, each grid represents the event and dynamics in the tissue. The graph on the *left* shows the causal path of the events. Each edge associated with plus (+) sign represents posi-

tive feedback to the vertex it is pointing on (activation, release/adding concentration, healing), while the one associated with negative sign (-) carries negative feedback (inhibition, damage)

where $z_1^t(x)$ is the epithelial cells state at time step t and location x , $z_{3TNF}^t(x)$ is concentration of pro-inflammatory cytokine (explained later) occupying the same grid coordinate, rand is random number generator based on beta function probability density, α_1 and β_1 are two beta function parameters, and $\text{samp}(w, d)$ is random sampling algorithm that samples data set d by weights w . Equation (10) describes the state transition by cytokine (TNF) and fibroblast (healing). The healing condition comes from cell mitosis and fibroblast, and is described by Eqs. (12) and (13) below.

$$\text{unirand} < P_{mt} \tag{12}$$

$$z_1^{t+th}(x) = 1 \text{ when } z_{2f}^t(x) = 2 \tag{13}$$

where unirand is uniform random number generator between 0 and 1, P_{mt} is mitosis rate, and z_{2f}^t is the state of immune cells grid. The mitosis rate defines the probabilistic rate of

mitosis, as part of self-healing process of the cells. Equation (11) describes state transition influenced by scarring (explained in Sect. 2.3.5). Function samp randomly chooses the state of a cell, d , with some bias w . In this case, d is the possible state the grid can have (i.e., 0 and 1). The weight w skews samp to choose state 1 according to the numbers of collagen deposits at vicinity. If Moore’s neighborhood is used, then maximum number of collagen deposits is 9.

2.3.2 Immune cells

The immune cells move according to the concentration gradient (chemotaxis). The grids can contain three states: 0, 1 and 2, representing nonexistence of cells, inactivated, activated and secondary state for the immune cells. A simple probabilistic model of cell motility is used here, i.e.,

$$a_2 = \text{samp}(U(x), z_3^t(x)) \tag{14}$$

$$z_2^{t+1}(x) |_{U(x)} = \begin{cases} 1, & \text{at } z_2^t(a_2) \\ 0, & \text{otherwise} \end{cases} \tag{15}$$

where $\text{samp}(w, d)$ has been used once again, with different terms regarding w and d . In this case, samp randomly choose local grid site according to neighborhood $U(x)$, and the choice is biased according to z_3^t , which is the state of cytokine grid at current cell location, x . Variables in Eq. (14) is as follow: $U(x)$ is Moores neighborhood function, $z_2^t(x)$ is the state of immune cells grid at time step t . There are two type of immune cells, the macrophages (agent of inflammation) and fibroblasts (agent of healing). The state transition of the grid is applied toward grid with state $z_2^t(x) > 0$ (the grid occupied by immune cells), and governed by rule as follows,

$$z_{2m}^{t+1}(x) = \begin{cases} 1, & t_{\text{top}} > \epsilon_{\text{pop}} \\ 2, & z_1^t = 1(\text{fibroblast}), \text{rand}(\alpha_2, \beta_2) < z_4^t(x)(\text{macrophage}) \\ 0, & \text{otherwise or if } t_{\text{im}} > \epsilon_{\text{im}} \end{cases} \tag{16}$$

where ϵ_{im} is the age of immune cells, $z_4^t(x)$ is the state of elastic field grid (which will be explained later) and the random number generation using beta function probability density has been used once again. Equation (15) is applied to both type of immune cells, with minor differences in details (including the rule for activation) as shown in Eq. (16). The macrophages are still mobile after activation, while fibroblast will stay at the last grid site after activation. The latter represent fibroblast differentiating at injured site. This means the rule in Eqs. (14) and (15) still applies to macrophages after activation, but not fibroblasts. In addition, the ϵ_{im} of fibroblast also reduced by 75% after activation.

When activated, the immune cells release cytokines. Each type of immune cell is associated with a specific cytokine (i.e., macrophage releases TNF, and fibroblast releases TGF). Macrophage tends to release TNF where the environment experiences more strain, while fibroblast tends to release TGF in the presence of TNF. However, TGF inhibits macrophage in releasing TNF. Hence, the CA reflects the activator-inhibitor system. The cytokines release by immune cells can generally be expressed as,

$$z_{3TNF}^{t+1}(x) = \begin{cases} 1, & \text{rand}(\alpha_3, \beta_3) \geq z_{3TGF}^t(x) \text{ when } z_{2m}^t(x) = 2 \\ 0, & \text{otherwise} \end{cases} \tag{17}$$

$$z_{3TGF}^{t+1}(x) = \begin{cases} 1, & \text{rand}(\alpha_4, \beta_4) \leq z_{3TNF}^t(x) \text{ when } z_{2f}^t(x) = 1 \\ 0, & \text{otherwise} \end{cases} \tag{18}$$

Table 3 Beta Function Parameters

Subscript number	Case	α	β
1	Epithelial cells grid (Eq. 6)	5	1
2	Macrophages activation (Eq. 11)	5	1
3	TNF release (Eq. 13)	1	3
4	TGF release (Eq. 14)	2	1

Table 4 CA parameters for simulation in this paper

Mitosis probability, P_{mt}	1/5
Healing time	5
Collagen time, K_c	10
Collagen dissolution	10%/tick
TNF diffusivity, D_{TNF}	0.07
TGF diffusivity, D_{TGF}	0.1
TNF dissolution constant, K_{TNF}	1E-3
TGF dissolution constant, K_{TGF}	1E-5
Repopulation of immune cells, ϵ_{pop}	5 ticks
Immune cells life time	20 ticks
Immune cells speed	3 cells/tick
Population of immune cells, n_{im}	25

where $z_3^t(x)$ is the state of cytokine grid at time t , the subscript denotes the type of cytokine, $z_2^t(x)$ is the state of immune cell grid at the same time step, and subscript m and f denote the type of immune cell (macrophage and fibroblast), consecutively, α and β are beta function parameters which are given in Table 3.

The population of immune cells is also kept at averagely n_{im} numbers, with 0.25 variance. This means the first condition in Eq. (15) applies at random grid location to ensure the population is at n_{im} on average. As before, the beta function and rules parameters are given in Tables 3 and 4.

2.3.3 Cytokine grid

The cytokine grid contains an array of CA cells to simulate the spread of cytokines by diffusion, and its disintegration over time. One way to simulate spread is to employ an additive rule such as,

$$z_3^{t+1}(x) = \Sigma_{U(x)} k_i z_3^t(x) \tag{19}$$

where k_i is a set of constant corresponding to neighborhood function, $U(x)$. To determine k_i , one may gain insights from a system appearing as a numerical solution of diffusion equations with additional disintegration terms,

$$\dot{C} = D\nabla^2 C - K \cdot C \tag{20}$$

where C is concentration, D is diffusivity, K is a constant determining the rate of disintegration. Numerical solution by Finite Difference Method gives,

$$z_3^{t+1}(x) = z_3^t(x) + D \Sigma_{U(x)} k_i z_3^t(x) - K z_3^t(x) \quad (21)$$

where Neumanns neighborhood is used, and cells have continuous state, and $k_i = 1 - 4D$ for $U(x) = 0$, and $k_i = D$ otherwise. As before, D and K are shown in Table 4.

2.3.4 Elastic field grid

It is theorized that mechanical strain on tissue activates ion channel(s) on the cells that leads to the release of an array of cytokines (Halbertsma et al. 2005). In this model, the mechanical strain is represented by another layer of CA grid as a discretized strain field. The FEM simulation in the study provides insights into the strain distribution. This is translated into the discretized distribution of strain fields in the CA grid. This strain field acts as an energy gradient in activating the immune cells. The model simplifies the activation process by ignoring the molecular mechanism of ion channels opening by strain and cell signaling pathways that lead to the release of specific cytokines. In addition, only the macrophage is activated by strain. The rule dictating macrophage activation is expressed in Eq. (16).

2.3.5 Scarring

The healing by fibroblasts release TGF that contributes to production of collagen. Hence, there is a surge of collagen concentration as a result of healing by fibroblasts. This introduces scar to the tissue, and reduce tissue compliance. In the present study, we represent this phenomenology where collagen deposits after healing add risks to damage on epithelial cells. In CA, the site of these collagen deposits are the same as the location of fibroblast after activation. The effect of these collagen deposits will stay after specified time, as shown Table 2 as collagen time. The rule of collagen deposits is as follow,

$$z_5^{t+t_h}(x) = \begin{cases} 1, & \text{at } z_{2f}^t(x) = 2 \\ 0, & \text{otherwise} \end{cases} \quad (22)$$

CA rules were implemented in MATLAB R2016. The statistical toolbox was used for random algorithms, rand and samp. The samp is basically a randomized data sampling algorithm, and MATLAB R2016 uses the algorithm provided by Wong and Easton (1980). The simulation is run for a domain representing tissue experiencing mechanical strain, expressed in elastic field grid of CA. The grids contain 100 by 100 cells, where a biologic epithelial cell size is around $1 \mu\text{m}$. The boundary condition used is periodic boundary

condition, where continuum between two opposite edge of the boundary is imposed as,

$$Z^t |_{\Gamma_1(x)} = Z^t |_{\Gamma_2(x)} \quad (23)$$

where Γ_1 and Γ_2 are set of two opposing boundaries.

3 Results and discussion

FSI is conducted on a 3D model of alveolar sac and three different values of TV (TV = 200, 500 and 1000 mL). Strain distributions are post-processed to investigate regions with highest concentration of strain. Next, strain versus time curves in different locations of the model are post-processed to evaluate effect of tidal volume on strain level changes during the breathing cycle. Then, maximum strain values from FSI are employed in the CA model. The CA model is implemented using MATLAB R2016A, and three commonly found strain distributions (uniform, middle trough and sinusoidal bumps strain distributions) are taken into consideration to explore the influence of different TVs in mechanical ventilation on cell population dynamics.

3.1 Strain distribution

Strain distributions are presented in Fig. 4 for different tidal volume values. As can be seen, higher strain is observed at the inlet area and increasing tidal volume leads to higher strain levels in the alveolar model. Initially, the alveolar model shows a slight contraction but the alveolar duct shows an expansion to let air enter into the alveolar region. Then, at the end of inspiration time, the alveolar volume will be filled with air and this process would again happen in the reverse direction, inlet duct contracts while alveolar region is expanding until air leaves the alveolar region and then the alveolar would return back to the nondeformed shape. This procedure is regarded as nonuniform deformation of alveolar wall (Gefen et al. 1999).

Three different types of strain distribution in alveolar region. As can be observed, strain in the center of alveoli is distributed uniformly but in each alveolus, it is concentrated in the connection of the alveolus to the neighbor alveoli, as compared to the center of the alveolus itself which is termed middle through strain distribution in this study. In addition, another strain distribution, defined as sinusoidal bumps, is distinguished on the connection edge of the alveoli where it is approximately distributed in symmetric form with a higher strain distribution. These three types of strain distributions are presented in Fig. 5.

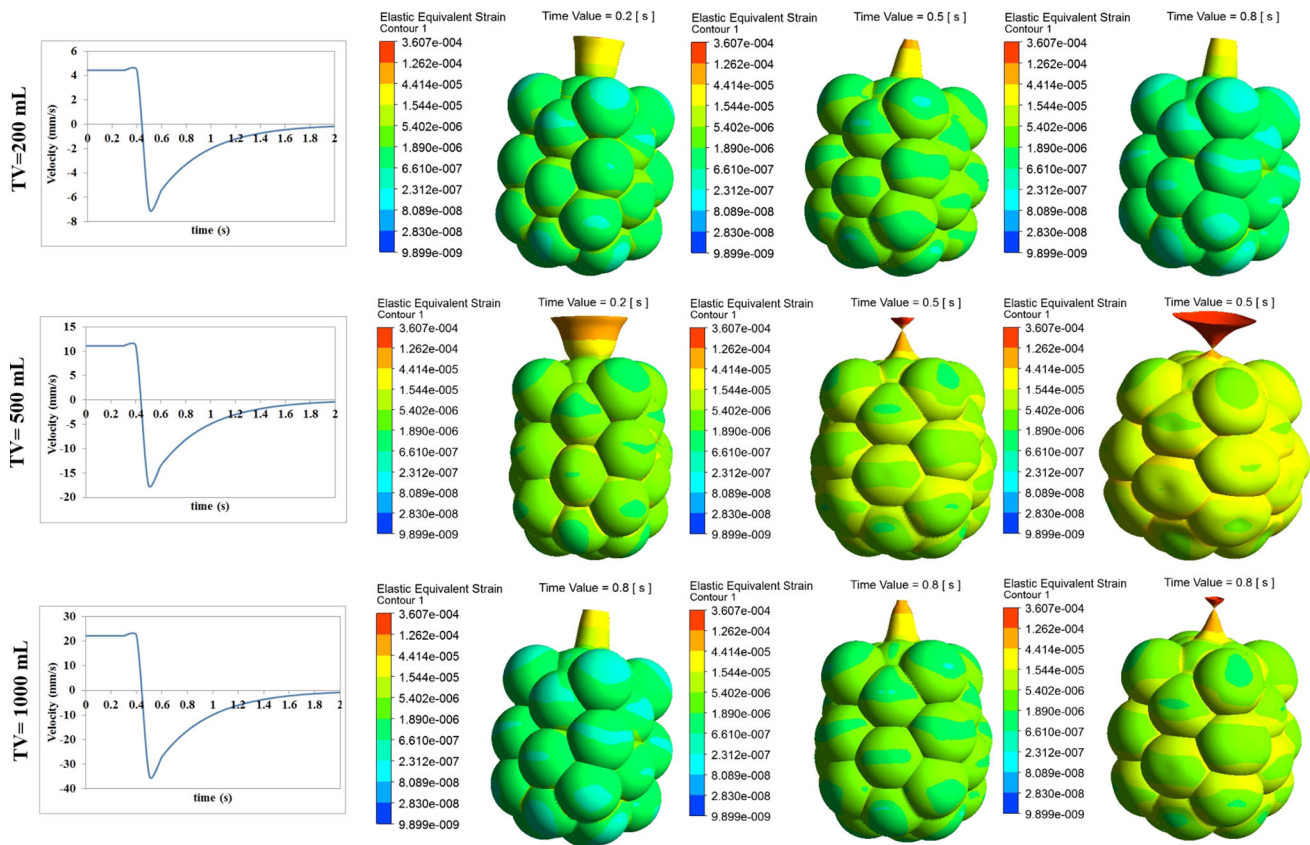


Fig. 4 Strain distribution at inhalation ($t = 0.2$ s) and exhalation time ($t = 0.5, 0.8$ and 2 s) for $TV = 200, 500$ and 1000 mL

3.2 Strain level at various regions in alveolar sacs

Strain versus time curves for different TVs are plotted at different locations in alveolar region and as it is illustrated in Fig. 6, max equivalent elastic strain value for tidal volume equal 500 mL is approximately 2 times bigger than strain value for 200 mL and 2 times smaller than strain value for 1000 mL. Also, it can be seen that middle layers in alveolar region represent higher strain level in comparison to upper and lower layers.

3.3 Sensitivity analysis

Sensitivity of strain level to changes in alveolar tissue's mechanical properties and wall thickness is examined. For this aim, shear and bulk modulus values are altered by 10 and 25% (reduction and increase compare to initial values). Sensitivity analyses is also conducted by reconstructing 10 times thicker and thinner alveolar wall thickness compare to initial model. As it was discussed earlier, middle layer would sustain higher strain level in alveolar model. Therefore, FSI results for different case studies for morphological changes with $TV = 500$ are compared at middle layer within alveolar model. Results presented that decreasing shear and bulk

modulus would lead to higher strain level within the alveolar model and in contrast, increasing discussed parameters reduce strain level in the model. It is observed that increasing and decreasing by 10 and 25% would correspondingly lead to 10 and 30% change in strain level and 10 times increased and decreased alveolar wall thickness would subsequently increase and reduce strain level by almost 10 times. Strain distributions, by contrast, are same for all case studies. In following results from FSI are imported in CA model.

3.4 Strain-induced inflammation simulation

The developed CA model was used to study the effect of different tidal volumes in mechanical ventilation on the cell population dynamics. Based on FSI analysis at the alveolar region, three commonly found strain distributions are taken into consideration for the cell population dynamics as shown in Fig. 5. Since we are interested in the percentage of parametric change, the simulation is carried out with normalized variables. Hence, the magnitude of strain is normalized with respect to the highest value of the three schemes as shown in Table 5. In addition, the time scale of cell population dynamics is remarkably higher than typically found in breathing

Fig. 5 Typical distribution of strain. The color bar on the right shows the magnitude correspond to the color plot. **a** Uniform, **b** middle trough and **c** sinusoidal bumps

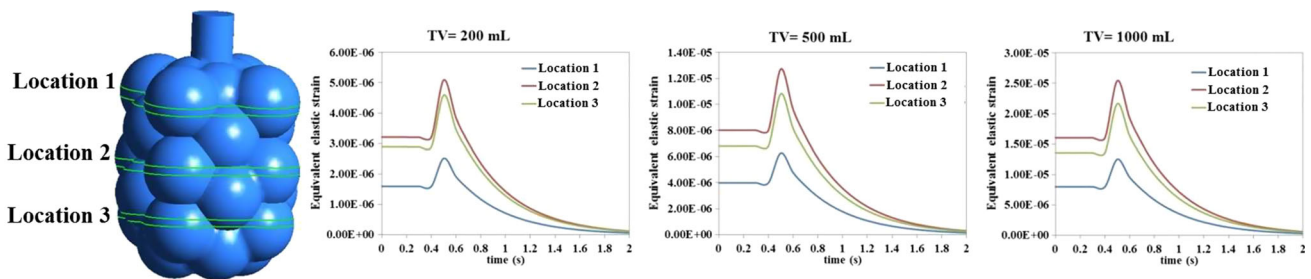
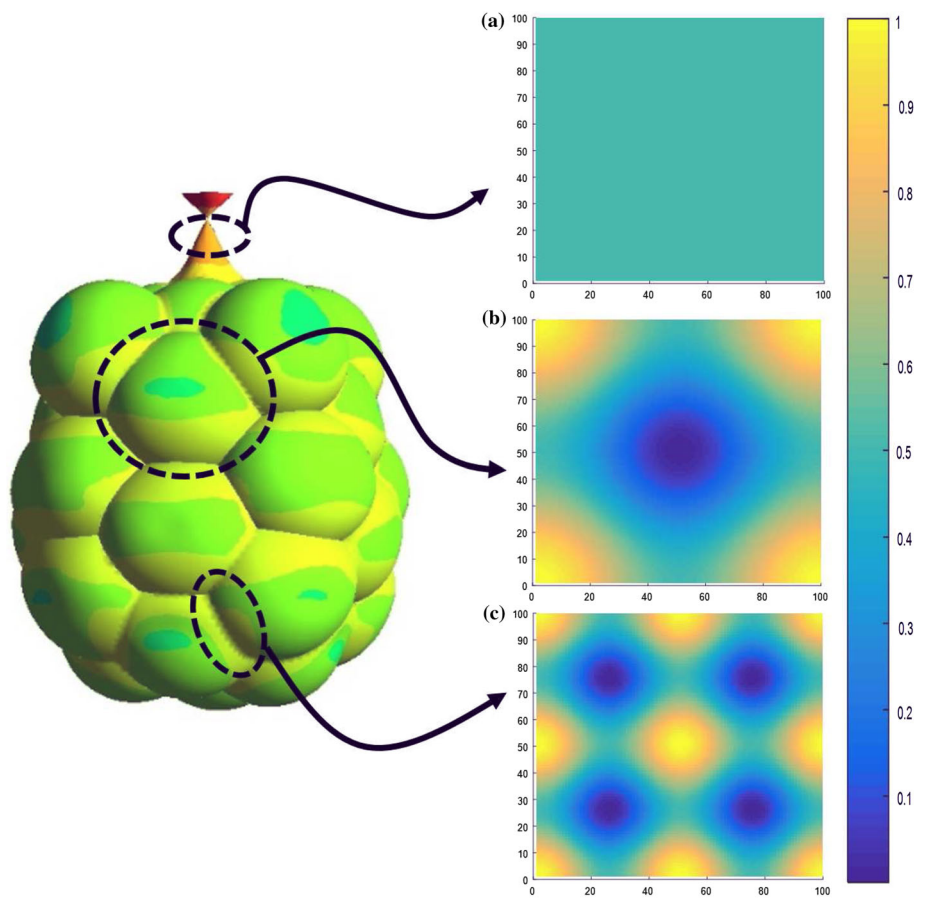


Fig. 6 Strain level alternation from location 1 to location 3 for different TVs

Table 5 Three schemes for CA simulation of cell population dynamics

TV (mL)	Real value	Normalization
200	2.4E-05	0.21
500	5.99E-05	0.52
1000	1.15E-04	1.00

cycle. Hence the justification is made for taking the amplitude of strain during the breathing cycle for this CA model.

3.4.1 Case study I (uniform strain)

FSI results suggest the cell population in the tissue experience some uniform level of strain. The amplitudes of strain

as shown in Table 5 were applied for the three strain distributions. Figure 7 shows numbers of dead epithelial cells and collagen deposited according to different level of strain. The numbers of dead epithelial cells can be seen as a measure of damage done in epithelium. Figure 7 also shows different trend of damage occurring on the tissue. Figure 7a shows a spike that last until approximately 600 simulation time, followed by smaller spike of damage. In Fig. 7b, the damage increased rapidly and the increasing trend stopped at approximately 100 simulation time. In Fig. 7c, the damage keeps increasing until 1000 simulation time. Notice that the CA grid has 10,000 cells in total, but the damage in case of Fig. 7c did not spread to the whole grid. The numbers of collagen deposits follow the trend of epithelium damage in

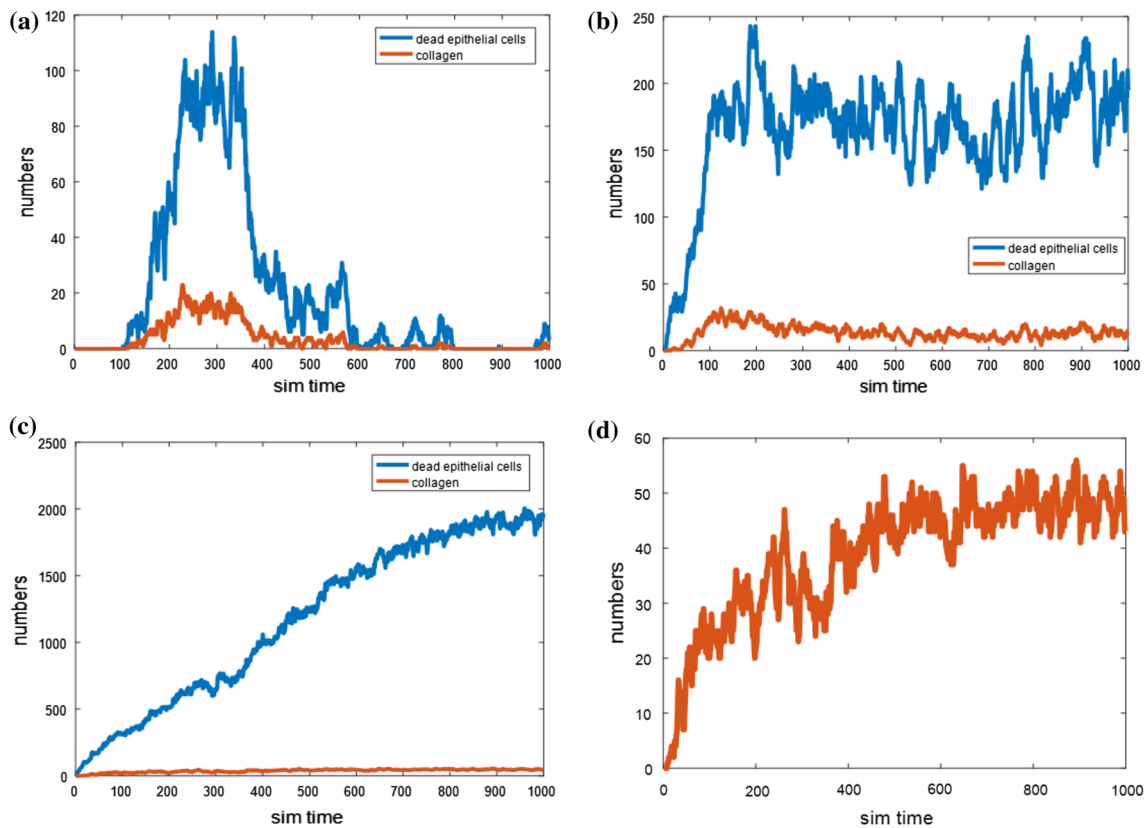


Fig. 7 Cell population dynamics corresponding to case study I; numbers of dead epithelial cells on, **a** norm. strain = 0.21, **b** norm. strain = 0.52, **c** norm. strain = 1, and **d** numbers of collagen deposits

Fig. 7a, b. However, in the case of Fig. 7c, the numbers of collagen deposits increase and tend to slow down at approximately 600 simulation time.

Figure 8a, b shows the spatial distribution of epithelium damage for the case shown in Fig. 7a at 300 and 550 simulation times, respectively. The damage in Fig. 8a corresponds to the spike damage in Fig. 7a, and it shows that the damage appeared in random locations as three patches on the tissue represented by CA grid. After 550 simulation time, the patches of damage reduced into only one of the previous three patches. Figure 8c shows the distribution of fibroblasts (yellow dots) and collagen deposits (dark dots). The fibroblasts are clearly distributed around the damage patches. Figure 8d shows the comparison of the peak damage occurring for the three strain magnitudes considered in this study. The increase in the peaks shows the exponential rise in damaged cells as the strain was increased.

Figure 9 shows the snapshots of damage distribution for the case illustrated in Fig. 7b. The damage in this case tended to be steady after approximately 100 simulation times. In Fig. 9a, the damage appeared at random locations as patches with an intact tissue after 180 simulation times. After 900 simulation times the patches shrank, but the damage was distributed more spatially with smaller patches. However, as can be seen in Fig. 7b, the damage seems to be steady.

3.4.2 Case study II (middle trough)

In this case, the peak strain surrounds an area of low strain. Figure 10 shows the dynamics of cell population under different strain amplitudes, which are the same as described in a previous section. Figure 10a shows two clear spikes of epithelium damage during the simulation time. Figure 10(b) shows peak damage that lasted longer than the previous one; this one is similar to the case in Fig. 7a. The case in Fig. 10c shows the tendency of constant increase in damage over time. As before, the collagen deposits in Fig. 10b showed a similar trend to epithelium damage. However, there is no collagen deposit in Fig. 10a, and collagen deposits in the last case as shown in Fig. 10c decreased and showed a tendency to stabilize after approximately 600 simulation times, despite the increasing damage to the epithelium.

Figures 11a, b shows spatial distributions of epithelium damage of the case shown in Fig. 10a. Figure 11a corresponds to the first spike in Fig. 10a at 67 simulation time, and Fig. 11b corresponds to the second spike at 444 simulation times. There is only one patch of damage with minimum numbers of dead cells. The spikes in Fig. 10a apparently correspond to two different locations of patches of damage. The location of patches, as should be expected, tends to appear in regions

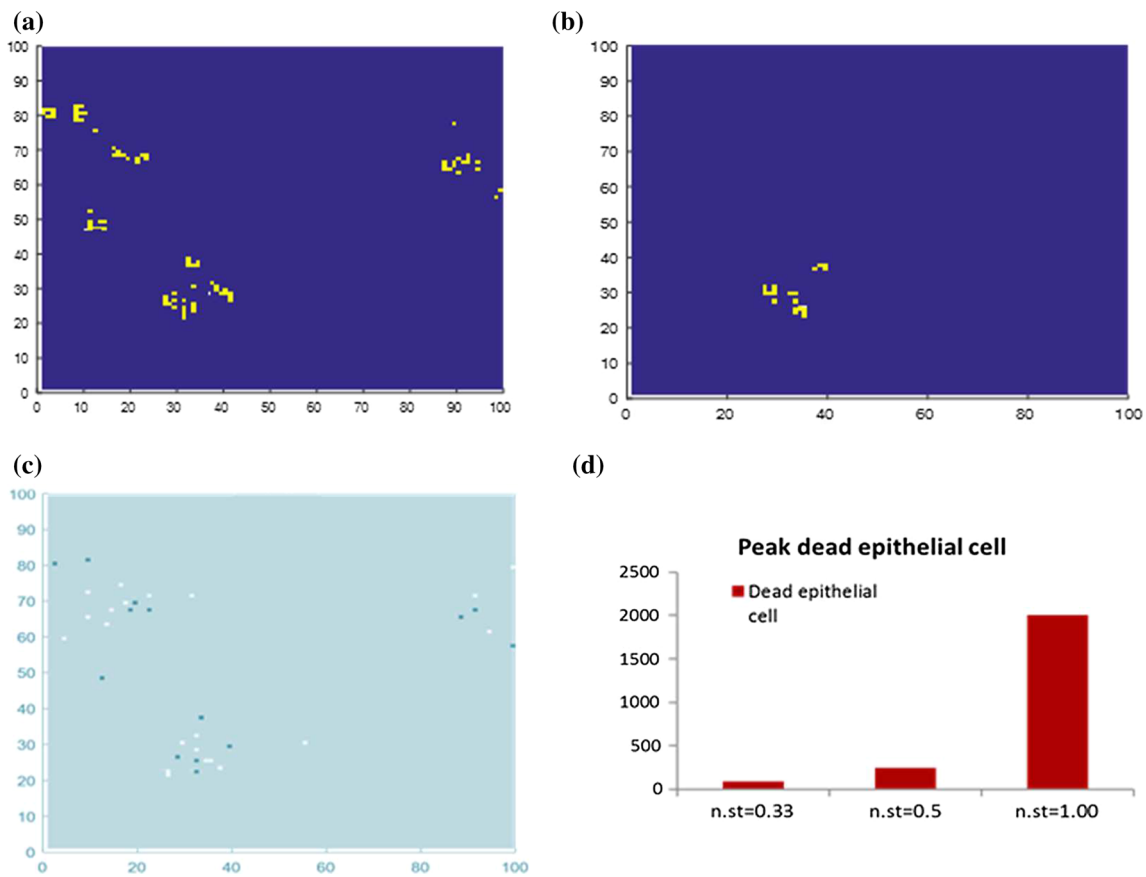


Fig. 8 **a** Epithelial cells damaged after 300 simulation times, *yellow-colored* grid denotes the portion of tissue with dead epithelial cells, **b** epithelial cells damaged after 550 simulation times, **c** fibroblasts (*white dots*) and collagen deposits (*dark dots*) and **d** peak damage to epithelium

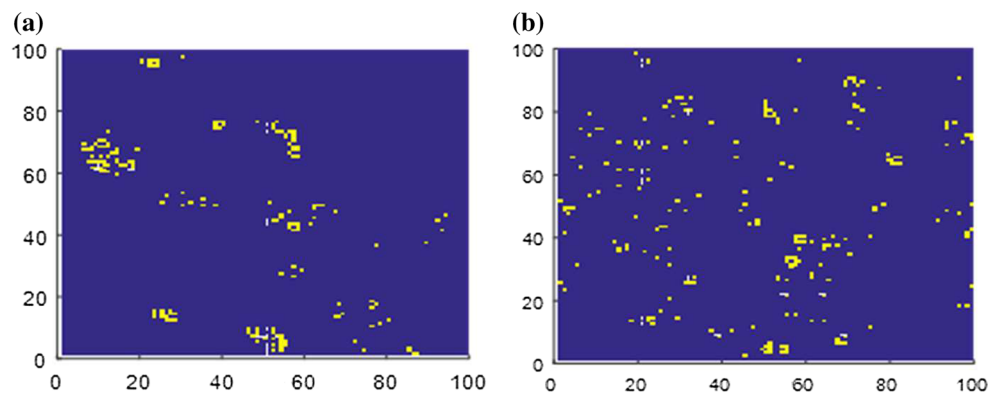


Fig. 9 Snapshots of case with norm strain = 0.52, **a** epithelial cells damages after 180 simulation time, *yellow-colored* grid denotes the portion of tissue with dead epithelial cells and **b** epithelial cells damages after 900 simulation time

close the amplitude of strain. Figure 11c shows fibroblasts distribution corresponding to the case shown in Fig. 10a at 67 simulation times (coinciding with the first spike). As can be seen, the fibroblasts are not concentrated in one place, and are spread out on the whole CA grid. Figure 11d shows the peak damage in the epithelium, as well as the exponential rise in damage as strain increased, similar to the previous case of uniform strain.

3.4.3 Case study III (sinusoidal bumps)

Figure 12 shows epithelium cells population dynamics under the strain distribution as shown in Fig. 5c. As shown in Fig. 12a, there is clearly no damage to the epithelium, despite some degree of damage that occurred in the previous case with the same strain amplitude. In Fig. 12b, we can see that the damage increased rapidly after 200

Fig. 10 Cell population dynamics corresponding to case study II ; numbers of dead epithelial cells on, **a** norm. strain = 0.21, **b** norm. strain = 0.52, **c** norm. strain = 1, and **d** numbers of collagen deposits

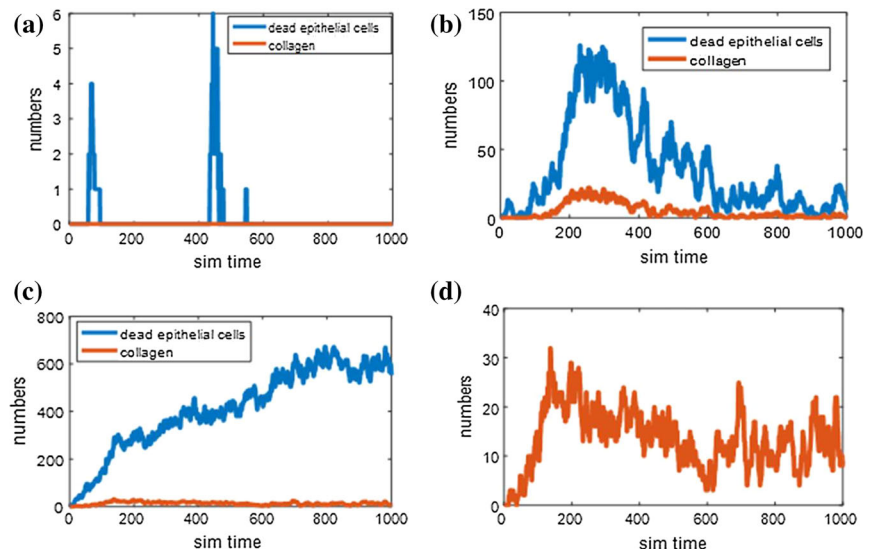
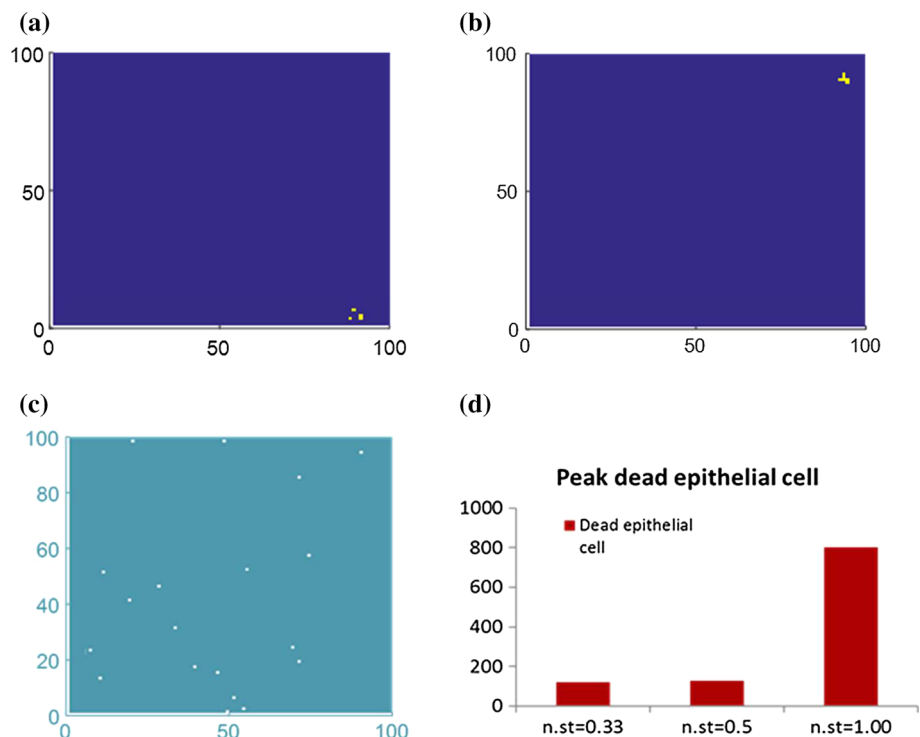


Fig. 11 **a** Epithelial cells damaged after 67 simulation times, *yellow-colored* grid denotes the portion of tissue with dead epithelial cells, **b** epithelial cells damaged after 444 simulation times, **c** fibroblasts (*white dots*) and **d** peak damage to epithelium



simulation times, but decreased after a short period of time. However, the damage did not vanish completely and some level of damage remained until the end of simulation time. Figure 12c shows population dynamics under the highest strain amplitude. The damage increased since the epithelium is subjected to the strain, and stabilized after approximately 500 simulation times. Figure 12d shows peak damage for this case, and it showed a similar exponential tendency as discussed in the previous two cases.

4 Discussion

FSI analysis is conducted on a symmetric alveolar sac model for three different tidal volume values. Strain distributions in the alveolar region were analyzed, and it was observed that the connection points of the alveoli undergo higher strain during the breathing cycle. While nonsymmetric model would generate more variations of strain distribution that may present nonuniform distribution similar to the considered symmetric alveolar sac model in this study. Additionally,

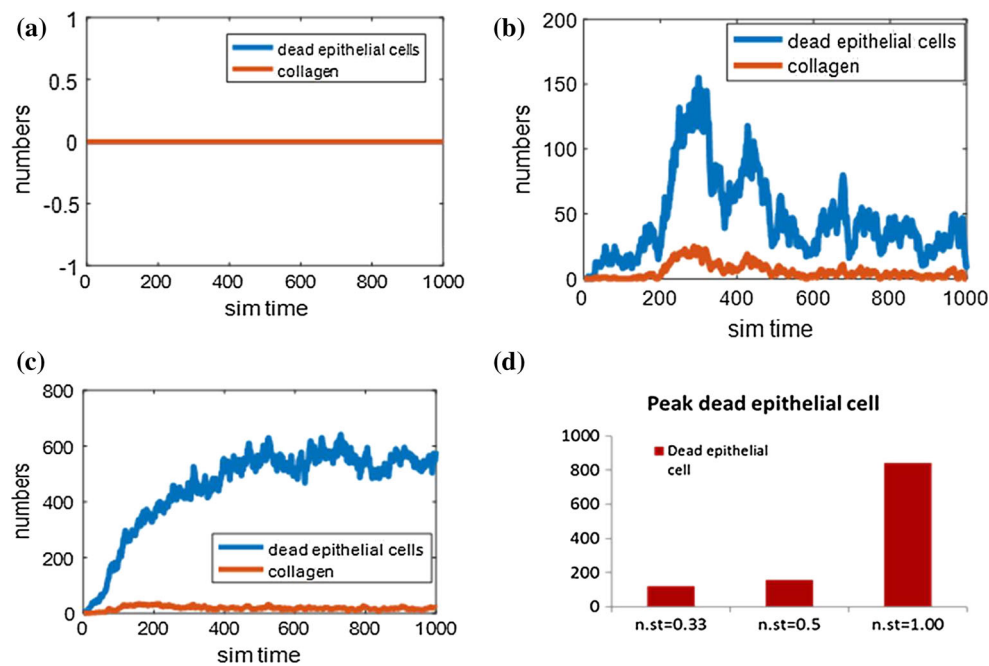


Fig. 12 Cell population dynamics corresponding to case study III; numbers of dead epithelial cells on, **a** norm. strain = 0.21, **b** norm. strain = 0.52, **c** norm. strain = 1, and **d** peak damage to epithelium

strain-time curves plotted for different tidal volumes at three different locations through the model showed that the middle layers would tolerate a higher level of strain in comparison to the upper and lower layers considered in the model. Sensitivity analysis shows that strain level in alveolar region is highly sensitive to alveolar sacs morphological changes in pulmonary acinar region, but it would not considerably change strain distribution. Three different strain distributions derived from post-processed FSI results were implemented in the CA model to investigate influence of tidal volume and strain level on cell population dynamics under the MV condition. The first case considered in the CA model clearly depicts that while the strain is low enough, the tissue is still able to sustain healing capacity by mitosis and fibroblasts eventually mitigate the damage. Increasing the TV (and hence, increasing strain), leads to reduction of healing capacity. Generally, the tissue is able to mitigate damage, but some amount of damage still persists. Furthermore, the simulations show that the strain distributions significantly impact the population dynamics of epithelial cells. It is interesting to note that the epithelium under the same amplitude of strain demonstrates specific population dynamics. This may be caused by the chances of macrophages exposed to strains of the tissue. The initial locations of macrophages are initially determined by uniform RNG. Although the macrophages are initially randomly distributed on the grid (and expectedly statistically uniform as the result of uniform RNG), it can be said that the strain distributions pose less risk of initially triggering inflammation by macrophages (that is, the release of TNF).

Increasing the strain amplitude will affect the chances of macrophages releasing TNF. The interplay between strain amplitude and distribution also influences the healing capacity of the tissue. The tissue and its constituents will still be able to reduce or withhold damage when the strain amplitude is low enough. However, when the strain distribution lowers the chance of the macrophages being exposed to strain, the tissue is still able to stop the rate of damage, although not reduce it. Snapshots of the spatial distribution of damage on the epithelium provide more insights into the inflammation. Generally, damage appears randomly as patches and these patches are reduced in number gradually by the healing effect which is influenced by fibroblasts (along with mitosis). As soon as one or a few fibroblasts are found in the location of a damage patch, the cell signaling by TNF will attract more fibroblasts that wander randomly on the grid. This prevents the damage from spreading and localizing. However, in the case of steady damage withholds, the damage at first appears as patches. Next, the patches are reduced by healing. However, more damage appears on different locations, leading to smaller and more distributed damage. In this case, the tissue constituents are not able to localize damages. Hence, the quantitative charts would not reveal the whole dynamics of the damage. Since, fibroblasts are cells with motility, and may not arrive at the damage locations, in the case which damage patch appeared after 67 simulation times in a region with higher strain amplitude. This patch quickly healed by mitosis as the fibroblasts which can be seen did not surround the location. After 444 simulation times, another spike appeared,

Table 6 Qualitative behavior of the alveolar tissue CA model when being subjected to strain at different level

Cases	Inflammation		
	Strain: 0.21	Strain: 0.52	Strain: 1.00
1: Uniform	Suppressed	Steady	Rising
2: Middle Trough	Spikes	Suppressed	Steady
3: Sinusoidal	Nonexistent	Suppressed	Steady

corresponding to another patch that appeared in a different location. From these snapshots, it can be inferred that as long as the damage patches can be healed quickly, the tissue and its constituents will still be able to revert back to intact tissue. Peak damage (assumed as the number of dead cells) in all the three cases in this study showed an exponential rise as strain amplitude increased, despite strain distribution. As expected, the uniform strain distribution had the highest damage. Results from the other two strain distributions suggested that they led to similar amounts of peak damage. It is well known that tissue integrity is influenced by the population of the cells. The quantitative comparison of the number of dead cells presented in this study can be used as a justification for analysis at the organ level. For instance, based on the results from this study, one could suggest an exponential function to find the changes in mechanical properties of tissue as a result of increasing TV in MV. It is to be noted that the collagen parameters only contribute to damaging airway tissue. It is also implied that collagen accumulation may contribute to increased airway impedance (Estrada and Chesler 2009), which can be reflected by alteration of airway tissue elasticity in the organ model. This will be included in future works. It must be acknowledged that the CA model presented needs experimental tuning, since it has only been compared qualitatively. However, the CA model has also been shown to address a variety of dynamic behavior, based on the abstraction of interaction of cells in tissue. Thus, the model has provided a framework for experimental tuning and parametric matching tools for studying the complex dynamics of inflammation.

Table 6 summarizes the qualitative behavior captured in the CA model based on the quantitative results. In this table, the inflammation score is defined as the number of dead epithelial cells. When inflammation rises and slows down after some time steps (such as in Case 1 with uniform 0.21 strain magnitude), the behavior is called suppressed. When the healing can maintain inflammation, it is called steady. And when healing function breaks down, it is termed rising. When inflammation is suppressed quickly by healing function, it is termed spikes. The summary clarifies that the immune response differs when the strain distribution is not uniform and strain distribution may play a role in the immune system overall. However, small or little bumps of strain on

the tissue apparently have minimal effect on the qualitative behavior of the immune response.

5 Conclusion

In this study, FSI analysis was employed to study strain levels in the alveolar region. This was followed by implementation of a CA model for strain-induced inflammation. It was observed that strain is highly concentrated in the inlet area. In addition, strain versus time curves in different locations through the alveolar model showed that middle layers in the alveolar region underwent higher level of strain during breathing in the MV condition. Three different types of strain distributions in the alveolar region were analyzed; uniform, middle through and sinusoidal bumps. Since the time scale of deformation for the alveolar model is largely different from the deformation at the tissue level, the results from the alveolar model were abstracted into the CA model. This information was used to study population dynamics of cell constituents of tissue under MV for different strain levels associated with different TVs: 200, 500 and 1000 mL. The CA model results suggest that strain distribution plays a significant role in population dynamics. They also implied that interplay between strain magnitude and distribution determines healing effectiveness. Lastly, results suggest that increasing TV leads to an exponential rise in damage on tissue by inflammation.

Acknowledgements The authors thank the NSF for support this research through a Grant CMMI-1430379.

References

- Aleman D, Pappalardo F, Pennisi M, Motta S, Bruscia V (2012) Combining cellular automata and lattice Boltzmann method to model multiscale avascular tumor growth coupled with nutrient diffusion and immune competition. *J Immunol Methods* 376(1):55–68
- ANSYS (2013) Workbench User's Guide—Portal De Documentacion De Software
- Birukov KG, Jacobson JR, Flores AA, Shui QY, Birukova AA, Verin AD, Garcia JG (2003) Magnitude-dependent regulation of pulmonary endothelial cell barrier function by cyclic stretch. *Am J Physiol Lung Cell Mol Physiol* 285:L785–L797
- Brown BN, Price IM, Toapanta FR, DeAlmeida DR, Wiley CA, Ross TM, Vodovotz Y (2011) An agent-based model of inflammation and fibrosis following particulate exposure in the lung. *Math Biosci* 231(2):186–196
- Bungartz H-J, Schfer M (2006) Fluid-structure interaction: modelling, simulation, optimisation, vol 1. Springer, New York
- Carnell PH, Vito RP, Taylor WR (2007) Characterizing intramural stress and inflammation in hypertensive arterial bifurcations. *Biomech Model Mechanobiol* 6:409–421
- Cavalcante FS, Ito S, Brewer K, Sakai H, Alencar AM, Almeida MP, Suki B (2005) Mechanical interactions between collagen and proteoglycans: implications for the stability of lung tissue. *J Appl Physiol* 98(2):672–679

- Chopard B, Droz M (2005) Cellular automata modeling of physical systems, vol 6. Cambridge University Press, Cambridge
- Clark AR, Burrowes KS, Tawhai MH (2010) Contribution of serial and parallel microperfusion to spatial variability in pulmonary inter- and intra-acinar blood flow. *J Appl Physiol* 108:1116–1126
- Copland IB, Kavanagh BP, Engelberts D, McKerlie C, Belik J, Post M (2003) Early changes in lung gene expression due to high tidal volume. *Am J Respir Crit Care Med* 168:1051–1059
- Dutta-Moscato J, Solovyev A, Mi Q, Nishikawa T, Soto-Gutierrez A, Fox IJ, Vodovotz Y (2014) A multiscale agent-based in silico model of liver fibrosis progression. *Front Bioeng Biotechnol* 2:18
- Ermentrout GB, Edelstein-Keshet L (1993) Cellular automata approaches to biological modeling. *J Theor Biol* 160(1):97–133
- Estrada KD, Chesler NC (2009) Collagen-related gene and protein expression changes in the lung in response to chronic hypoxia. *Biomech Model Mechanobiol* 8:263–272
- Fluent A (2011) 14.0 Tutorial Guide ANSYS Inc, Canonsburg
- Foda HD, Rollo EE, Drews M, Conner C, Appelt K, Shalinsky DR, Zucker S (2001) Ventilator-induced lung injury upregulates and activates gelatinases and EMMPRIN: attenuation by the synthetic matrix metalloproteinase inhibitor, Prinomastat (AG3340). *Am J Respir Cell Mol Biol* 25:717–724
- Gefen A, Elad D, Shiner R (1999) Analysis of stress distribution in the alveolar septa of normal and simulated emphysematic lungs. *J Biomech* 32:891–897
- Haefeli-Bleuer B, Weibel ER (1988) Morphometry of the human pulmonary acinus. *Anat Rec* 220:401–414
- Halbertsma F, Vaneker M, Scheffer G, Van der Hoeven J (2005) Cytokines and bio-trauma in ventilator-induced lung injury: a critical review of the literature. *Neth J Med* 63:382–392
- Harding EM Jr, Robinson RJ (2010) Flow in a terminal alveolar sac model with expanding walls using computational fluid dynamics. *Inhal Toxicol* 22:669–678
- Haseneen NA, Vaday GG, Zucker S, Foda HD (2003) Mechanical stretch induces MMP-2 release and activation in lung endothelium: role of EMMPRIN. *Am J Physiol Lung Cell Mol Physiol* 284:L541–L547
- Kolanjiyil AV, Kleinstreuer C (2013) Nanoparticle mass transfer from lung airways to systemic regions-part I: whole-lung aerosol dynamics. *J Biomech Eng* 135:121003
- Kuebler WM et al (2003) Stretch activates nitric oxide production in pulmonary vascular endothelial cells in situ. *Am J Respir Crit Care Med* 168:1391–1398
- Li L-F et al (2003) Stretch-induced IL-8 depends on c-Jun NH2-terminal and nuclear factor-B-inducing kinases. *Am J Physiol Lung Cell Mol Physiol* 285:L464–L475
- Li L-F, Yu L, Quinn DA (2004) Ventilation-induced neutrophil infiltration depends on c-Jun N-terminal kinase. *Am J Respir Crit Care Medicine* 169:518–524
- Liu Y, So R, Zhang C (2002) Modeling the bifurcating flow in a human lung airway. *J Biomech* 35:465–473
- Mascarenhas MM et al (2004) Low molecular weight hyaluronan from stretched lung enhances interleukin-8 expression. *Am J Respir Cell Mol Biol* 30:51–60
- Moriyama K et al (2004) Enhancement of the endotoxin recognition pathway by ventilation with a large tidal volume in rabbits. *Am J Physiol Lung Cell Mol Physiol* 286:L1114–L1121
- Oudin S, Pugin J (2002) Role of MAP kinase activation in interleukin-8 production by human BEAS-2B bronchial epithelial cells submitted to cyclic stretch. *Am J Respir Cell Mol Biol* 27:107–114
- Precharattana M, Triampo W (2014) Modeling dynamics of HIV infected cells using stochastic cellular automaton. *Phys A* 407:303–311
- Pugin J, Dunn I, Jolliet P, Tassaux D, Magnenat J-L, Nicod LP, Chevrolet J-C (1998) Activation of human macrophages by mechanical ventilation in vitro. *Am J Physiol Lung Cell Mol Physiol* 275:L1040–L1050
- Reynolds A, Koombua K, Pidaparti RM, Ward KR (2012) Cellular automata modeling of pulmonary inflammation. *Mol Cell Biomech* 9(2):141–156
- Tanabe Y, Saito M, Ueno A, Nakamura M, Takeishi K, Nakayama K (2000) Mechanical stretch augments PDGF receptor expression and protein tyrosine phosphorylation in pulmonary artery tissue and smooth muscle cells. *Mol Cell Biochem* 215:103–113
- Tang S, Li Y, Yang Y, Guo Z (2015) The effect of mechanical-driven volumetric change on instability patterns of bilayered soft solids. *Soft Matter* 11:7911–7919
- Uhlig U, Haitsma J, Goldmann T, Poelma D, Lachmann B, Uhlig S (2002) Ventilation-induced activation of the mitogen-activated protein kinase pathway. *Eur Respir J* 20:946–956
- Uhlig S, Uhlig U (2001) Molecular mechanisms of pro-inflammatory responses in overventilated lungs. *Recent Res Dev Respir Crit Care Med* 1:49–58
- Weibel ER (1964) Morphometrics of the lung. *Handb Physiol Respir* 1:285–307
- Wiechert L, Metzke R, Wall WA (2009) Modeling the mechanical behavior of lung tissue at the microlevel. *J Eng Mech* 135(5):434–438
- Wong C-K, Easton MC (1980) An efficient method for weighted sampling without replacement. *SIAM J Comput* 9:111–113